Elucidating differences between carbon paper and carbon cloth in polymer electrolyte fuel cells

Yun Wang [a,1], Chao-Yang Wang [a,*], K.S. Chen [b]

[a] Electrochemical Engine Center (ECEC), Department of Mechanical and Nuclear Engineering,
The Pennsylvania State University, University Park, PA 16802, USA
[b] Engineering Sciences Center, Sandia National Laboratories, Albuquerque, NM 87185-0834, USA

Abstract

This paper seeks to develop a structure–performance relationship for gas diffusion layers (GDLs) of polymer electrolyte fuel cells (PEFCs), and hence to explain the performance differences between carbon paper (CP) and carbon cloth (CC). Three-dimensional simulations, based on a two-phase model with GDL structural information taken into account, are carried out to explore the fundamentals behind experimentally observed performance differences of the two carbon substrates, i.e. CC and CP, under low- and high-humidity operations. Validation against polarization data is made under both operating conditions, and the results indicate that the CC is the better choice as a GDL material at high-humidity operations due to its low tortuosity of the pore structure and its rough textural surface facilitating droplet detachment. However, under dry conditions, the CP shows better performance due to its more tortuous structure, which prevents the loss of product water to dry gas streams, thus increasing the membrane hydration level and reducing the ohmic loss. The present work is one step toward developing a science-based framework for selection of materials for next-generation, high-performance gas diffusion media.
© 2006 Elsevier Ltd. All rights reserved.

Keywords: Polymer electrolyte fuel cell; Modeling; Two-phase flow; Carbon cloth; Carbon paper

1. Introduction

Research on polymer electrolyte fuel cells (PEFCs) has been a rapidly growing field [1]. Among the PEFC components, the gas diffusion layer (GDL) plays an important role of electronic connection between the bipolar plate with channel-land structure and the electrode. In addition, the GDL also performs the following essential functions: passage for reactant transport and heat/water removal, mechanical support to the membrane electrode assembly (MEA), and protection of the catalyst layer from corrosion or erosion caused by flows or other factors [2,3]. Physical processes in GDLs, in addition to diffusive transport, include bypass flow induced by in-plane pressure difference between neighboring channels [4,5], through-plane flow induced by mass source/sink due to electrochemical reactions [6,7], heat transfer

[8,9] like the heat pipe effect [10], two-phase flow [10–13], and electron transport [14,15].

Two types of GDLs are commonly used in PEFCs: carbon paper [16–18] and carbon cloth [19–21]; both are commercially available. For convenience, carbon paper and carbon cloth are denoted as CP and CC, respectively, in the present paper. Both of them are carbon-fiber-based porous materials: carbon paper is non-woven, while carbon cloth is woven fabric, thus no binder is needed. Fig. 1 shows scanning electron microscope (SEM) pictures of these two GDL substrates. It has been experimentally observed that the performance of PEFCs employing CC GDLs is different from that with CP GDLs under low- or high-humidity operations, respectively [22–24]. Ralph et al. [22] showed that the CC indicates a much better performance than the CP at high current density operations (>0.5 A/cm^2) with internal humidification. Williams et al. [23] presented a characterization study on the properties of both commercial and in-house GDL substrates, including limiting current, electronic resistance, fraction of hydrophobic pores, gas permeability, pore size distribution, and morphology. Their experimental results indicated that CC

* Corresponding author. Tel.: +1 814 863 4762; fax: +1 814 863 4848.
  E-mail address: cxw31@psu.edu (C.-Y. Wang).
[1] Present address: Department of Mechanical and Aerospace Engineering, University of California at Irvine, Irvine, CA 92697-3975, USA.
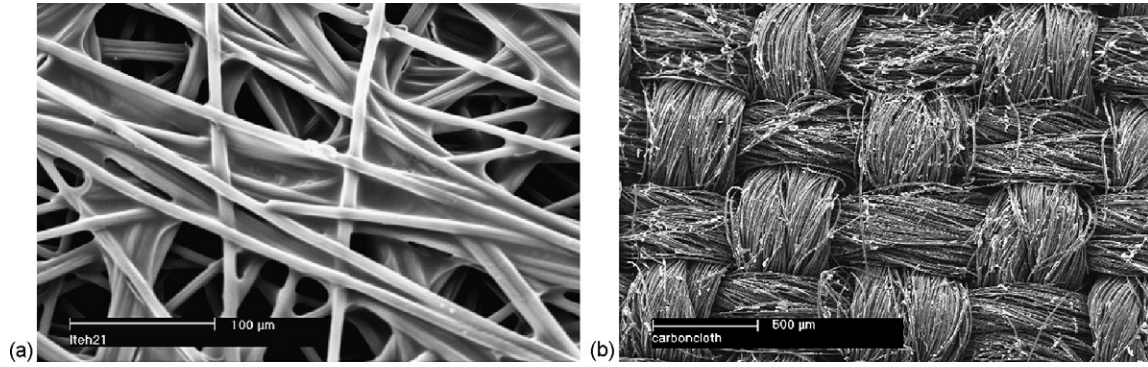
Fig. 1. SEM micrographs of: (a) carbon paper and (b) carbon cloth.

and CP show different performance at the atmospheric pressure operation. Similar result was also presented by Frey and Linardi [24]. However, no detailed explanation has been given as to why? More fundamentally, a relationship between GDL microstructure and performance is absent in the current literature.

This paper seeks to develop the structure–performance relationship for GDLs, and hence to delineate the differences between carbon paper and carbon cloth observed experimentally. In addition, this study makes a first attempt to incorporate the GDL structural information into a fuel cell model. Validation of the simulation results is presented at both dry- and humid-operations, together with an explanation by detailed distributions of species concentration and current density. The long-term goal of this work is to shed light on what structural properties are desired for next-generation, high-performance GDLs.

2. Physical and numerical model

The voltage loss of a PEFC is controlled by activation, Ohmic resistance, and mass transport. Under the isothermal condition, the mechanisms behind these losses are described by four principles of conservation: mass, momentum, species and charge, which, for the steady state, can be written in a concise form as follows [10,12,25]:

Continuity equation : $\nabla \cdot (\rho \vec{u}) = 0$ (1)

Momentum conservation : $\frac{1}{\varepsilon^2} \nabla \cdot (\rho \vec{u} \vec{u}) = -\nabla P + \nabla \cdot \rho \tau$
$$+ S_u \quad (2)$$

Species conservation : $\nabla \cdot (\gamma_c \vec{u} C^k) = \nabla \cdot (D_g^{k,\text{eff}} \nabla C_g^k)$
$$- \nabla \cdot \left[\left(\frac{m f_1^k}{M^k} - \frac{C_g^k}{\rho_g} \right) \vec{j}_1 \right] + S_k \quad (3)$$

Electron conservation : $0 = \nabla \cdot (\sigma^{\text{eff}} \nabla \Phi_s) + S_{\phi_s}$ (4)

Proton conservation : $0 = \nabla \cdot (\kappa^{\text{eff}} \nabla \Phi_e) + S_{\phi_e}$ (5)

where ρ, $\vec{u}$, p, C^k, Φ_s, and Φ_e, respectively, denote the density, superficial fluid velocity vector, pressure, molar concentration of species k, electronic phase potential, and electrolyte phase

potential. The assumptions made in the present model are as follows: (1) ideal gas mixtures; (2) isotropic and homogeneous membrane, catalyst layers and gas diffusion layers; (3) incompressible and laminar flow due to small pressure gradients and flow velocity; and (4) negligible mass source/sink in the continuity equation as justified in Ref. [7]. The physical, transport, and electrochemical properties as well as the source terms, S_u, S_k, S_{ϕ_e}, and S_{ϕ_s}, are summarized in Tables 1–3 in detail. Discussion of these property relations has been presented previously and is therefore not repeated here. Other properties related to two-phase dynamics and transport phenomena in the porous media are elaborated below.

2.1. Two-phase transport

The two-phase mixture density is defined as:

$$\rho = s\rho_l + (1 - s)\rho_g \quad (6)$$

where the liquid water saturation, s, is the volume fraction of open pores occupied by liquid water. In the M^2 (multiphase mixture) formulation [26], the liquid saturation is obtained from the following relation with the mixture water concentration, C^{H_2O}, after the latter is solved from the differential Eq. (3):

$$s = \frac{C^{H_2O} - C_{\text{sat}}}{\rho_l / M^{H_2O} - C_{\text{sat}}} \quad (7)$$

The flow fields of both phases in the GDL are described through the relative permeabilities, k_{rl} and k_{rg}, defined as the ratio of the intrinsic permeability of liquid and gas phases, respectively, to the total intrinsic permeability of a porous medium. Physically, it describes the extent to which one fluid is hindered by others in pore spaces and hence can be formulated as a function of liquid saturation. A set of functions have been used for the carbon-fiber-based porous media in the following power law:

$$k_{rl} = s^{n_k} \quad \text{and} \quad k_{rg} = (1 - s)^{n_k} \quad (8)$$

Berning and Djlali [27] set $n_k = 1$ in their work while most of others [10,12,13], including this work, used $n_k = 3$. Note that the larger n_k is chosen, the greater resistance liquid flow experiences. The presence of liquid phase affects the transport of species through the convection corrector factor, γ_c, and effective gas

Table 1
Physical and transport properties

| Quantity	Value
Water saturate concentration, $C_{sat}(T)$ [35]	$C_{sat}(T) = P^{sat}(T)/RT$, where $\log_{10} p^{sat} = -2.1794 + 0.02953$ $(T - 273.15) - 9.1837 \times 10^{-5} (T - 273.15)^2 + 1.4454 \times 10^{-7} (T - 273.15)^3$
Water content in membrane, λ [35]	$\lambda = \begin{cases} 0.043 + 17.81a - 39.85a^2 + 36.0a^3, & \text{for } 0 < a \leq 1 \\ 14 + 1.4(a - 1), & \text{for } 1 \leq a \leq 3 \\ 16.8, & \text{for } 3 \leq a \end{cases}$
Ionic conductivity of membrane, κ [35]	$(0.005139\lambda - 0.00326) \exp[1268(1/303 - 1/T)]$
H_2O diffusivity in membrane, D_w^m [36]	$D_w^m = \begin{cases} 3.1 \times 10^{-3}\lambda(e^{0.28\lambda} - 1) \times e^{-2436/T}, & \text{for } 0 < \lambda \leq 3 \\ 4.17 \times 10^{-4}\lambda(1 + 161e^{-\lambda}) \times e^{-2436/T}, & \text{otherwise} \end{cases}$
Electro-osmosis coefficient, n_d [37]	$n_d = \begin{cases} 1.0, & \text{for } \lambda \leq 14 \\ \dfrac{1.5}{8}(\lambda - 14) + 1.0, & \text{otherwise} \end{cases}$
Membrane density, ρ [38]	$\rho = \dfrac{1.98 + 0.0324\lambda}{1 + 0.0648\lambda} \times 10^3$
Diffusivity in the gas channels, D [39]	$D_o \left(\dfrac{T}{353}\right)^{3/2} \left(\dfrac{1}{p}\right)$
H_2/H_2O diffusivity in anode gas at standard condition, $D_{o,H_2,a}/D_{o,w,a}$	$1.1028 \times 10^{-4}/1.1028 \times 10^{-4}$ m²/s
O_2/H_2O diffusivity in cathode gas at standard condition, $D_{o,O_2,a}/D_{o,w,a}$	$3.2348 \times 10^{-5}/3.89 \times 10^{-5}$ m²/s
Viscosity of anode/cathode gas, μ [40]	$\mu = 9.88 \times 10^{-6} X_{H_2} + 1.12 \times 10^{-5} X_{H_2O} + 2.01 \times 10^{-5} X_{N_2} + 2.3 \times 10^{-5} X_{O_2}$

Table 2
Source terms for the conservation equations in each region

	S_u	S_k	S_{ϕ_e}	S_{ϕ_s}
Gas channels	0	0	–	0
Diffusion layers	$-\dfrac{\mu}{K_{GDL}}\vec{u}$	0	0	0
Catalyst layer	$-\dfrac{\mu}{K_{CL}}\vec{u}$	$-\nabla \cdot \left(\dfrac{n_d}{F} i_e\right) - \dfrac{s_k j}{n_k F}$	j	$-j$
Membrane	–	0	0	–

Electrochemical reaction:

$$\sum_k s_k M_k^z = ne^-, \quad \text{where} \quad \begin{cases} M_k \equiv \text{chemical formula of species } k \\ s_k \equiv \text{stoichiometry coefficient} \\ n \equiv \text{number of electrons transferred} \end{cases}$$

In PEM fuel cells, there are:
(Anode) $H_2 - 2H^+ = 2e^-$
(Cathode) $2H_2O - O_2 - 4H^+ = 4e^-$
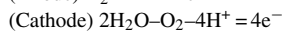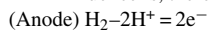
Note: n_d is the electro-osmotic drag coefficient for water. For H_2 and O_2, $n_d = 0$.

Table 3
Electrochemical properties

Description	Anode	Cathode
Transfer current density, j (A/m³)	$ai_{0,a} \left(\dfrac{C^{H_2}}{C_{ref}^{H_2}}\right)^{1/2} \left(\dfrac{\alpha_a + \alpha_c}{RT} \cdot F \cdot \eta\right)$	$-ai_{0,c} \left(\dfrac{C^{O_2}}{C_{ref}^{O_2}}\right) \exp\left(-\dfrac{\alpha_c F}{RT} \cdot \eta\right)$
Surface overpotential, η (V)	$\Phi_s - \Phi_e - U_o$	$\Phi_s - \Phi_e - U_o$
Equilibrium potential, U_o (V)	0	$1.23 - 0.9 \times 10^{-3}(T - 298)$
Exchange current density × reaction surface area, a_0i_0 (A/m³)	1.0×10^9	3.5×10^4
Transfer coefficient, α	$\alpha_a + \alpha_c = 2$	$\alpha_c = 1$

phase diffusivity, $D_g^{k,\text{eff}}$:

$$\gamma_c = \begin{cases} \dfrac{\rho}{C^{\text{H}_2\text{O}}} \left(\dfrac{\lambda_l}{M^{\text{H}_2\text{O}}} + \dfrac{\lambda_g}{\rho_g} C_{\text{sat}} \right), & \text{for water} \\[3mm] \dfrac{\rho \lambda_g}{\rho_g (1-s)}, & \text{for other species} \end{cases} \quad (9)$$

where λ_k is the relative mobilities of individual phases. Physically, the relative mobility describes the ratio of interface velocities or slip between gas and liquid water phases and can be formulated through liquid water saturation and the kinematic viscosity of phases:

$$\lambda_l = \frac{k_{rl}/v_l}{k_{rl}/v_l + k_{rg}/v_g} \quad \text{and} \quad \lambda_g = 1 - \lambda_l \quad (10)$$

Expression of $D_g^{k,\text{eff}}$ will be given in the later. The capillary diffusion flux, $\vec{j}_l$, in Eq. (3) can be calculated by:

$$\vec{j}_l = \frac{\lambda_l \lambda_g}{v} K [\nabla P_c + (\rho_l - \rho_g)\vec{g}], \quad \text{where}$$

$$P_c = P_g - P_l = \sigma \cos(\theta_c) \left(\frac{\varepsilon}{K} \right)^{1/2} J(s) \quad (11)$$

Here, σ is the surface tension, and $J(s)$ is the Leverett function, an empirical relation that is generally adopted for both hydrophobic and hydrophilic GDLs:

$$J(s) = \begin{cases} 1.417(1-s) - 2.120(1-s)^2 + 1.263(1-s)^3, & \text{for } \theta_c > 90° \\ 1.417s - 2.120s^2 + 1.263s^3, & \text{for } \theta_c < 90° \end{cases} \quad (12)$$

Usually, the GDL materials are made hydrophobic through adding PTFE to facilitate the water removal. The PTFE loading, commonly ranging from 5 to 30%, has significant influence on the contact angle, θ_c [2]. High PTFE loadings have been studied in Refs. [16,28].

The presence of liquid water in the catalyst layer will reduce the electrochemically active area. The following empirical formula is used to account for the effect of liquid water coverage [29]:

$$a = (1-s)^{\tau_c} a_0 \quad (13)$$

2.2. Carbon paper (CP) versus carbon cloth (CC)

The structural differences (non-woven versus interwoven), as shown in Fig. 1, result in two major quantifiable differences. One is that carbon cloth is more porous and less tortuous than carbon paper. The second is in liquid water coverage on the GDL surface, with carbon cloth being rougher and hence less liquid water coverage than carbon paper, as clearly shown in Fig. 2.

For gas phase transport, the effective gas diffusion coefficient in Eq. (3), accounting for the tortuosity, τ, is given by:

$$D_g^{k,\text{eff}} = \frac{\varepsilon}{\tau} D_g^k = \varepsilon^{\tau_d} D_g^k \quad (14)$$

where the Bruggeman factor, τ_d, is constant reflecting tortuosity for a specific porous media. Note that the last term in Eq.
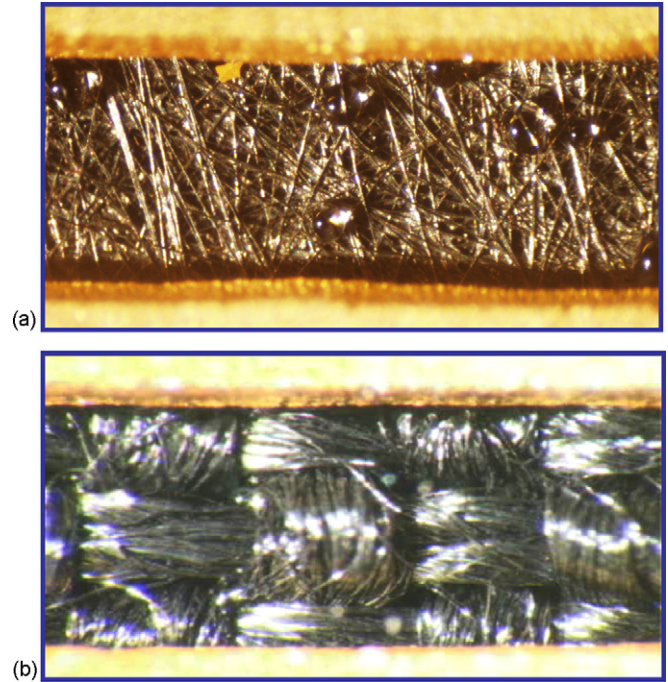

Fig. 2. In situ images of liquid water on GDL surface in operating PEFCs at 0.8 A/cm², 80 °C and 2 atm: (a) carbon paper and (b) carbon cloth. The channels shown are 1 mm wide, with droplets on carbon paper being ∼200 μm and those on carbon cloth ∼10 μm.

(14) is also referred to as Bruggeman relation. In previous work [9,12,30], the Bruggeman factor, τ_d, is set to be a constant at 1.5. For two-phase transport, the liquid water attaches on the pores' wall, following the same morphology of the GDL solid matrix. Thus, the effective gas diffusion coefficient is modified by:

$$D_g^{k,\text{eff}} = [\varepsilon(1-s)]^{\tau_d} D_g^k \quad (15)$$

In the present work, CP and CC are differentiated by their tortuosity factors that are fitted with experimental data (see Table 4).

Table 4
Geometrical and operating parameters

Quantity	Value
Gas channel depth/width (mm)	0.5/1.0
Shoulder width (mm)	1.0
GDL thickness, δ_{GDL} (mm)	0.2
Catalyst layer thickness, δ_{CL} (mm)	0.01
Membrane thickness, δ_m	0.03
Fuel cell height/length (mm)	2.0/100.0
Anode/cathode pressures, P (atm)	2.0/2.0
Stoichiometry, ξ_a/ξ_c	4.0/4.0
Temperature of fuel cell, T (K)	353.15
Porosity of GDL, ε	0.6
Porosity of catalyst layers, ε_g	0.4
Volume fraction of ionomer in catalyst layers, ε_m	0.2
Surface tension, liquid–water–air (80 °C), σ (N/m)	0.0625
Tortourosity of GDL (carbon paper/carbon cloth), τ	2.75/1.11
Liquid water coverage (carbon paper/carbon cloth), s_0 (%)	10/0
Effective electronic conductivity in the GDL/land, σ^{eff} (S/m)	500/20000
Contact angle, θ_c (°)	110
Permeability of GDL, K_{GDL} (m²)	10^{-12}

In addition, liquid water coverage on GDL surface, i.e. liquid water emerges from the porous GDL in the form of droplets, has great influence on the PEFC performance. Decreasing the coverage will benefit the oxygen access to the catalyst site. Several factors affect the attachment of water droplets on the hydrophobic GDL surface, they are gas flow rate in the channel, GDL surface roughness, water production rate, and contact angle [31,32]. The gravitational effect can be neglected considering the dimension of droplet diameter is small, <1 mm. A general approach to modeling liquid water coverage on GDL surface has been outlined by Meng and Wang [29]. For simplicity, in the present work we use a constant interfacial coverage, i.e. $s_0 \approx 10\%$ and 0% for CP and CC, respectively. These values were estimated from video files of droplet visualization on GDL surface in operating fuel cells obtained in our laboratory (not included here).

Key parameters characterizing the CC and CP are listed in Table 4. The values of permeability, K, contact angle, θ_c, electronic conductivity, σ^{eff}, and porosity, ε are selected for typical GDL materials, which are set to be the same for the CC and CP due to the negligible differences under the same PTFE loading. In addition, in our experiments performed for model validation, good care has been taken to make identical conditions for the CC and CP, such as the PTFE loading and compression, thus the differences observed can be solely ascribed to the structural features of the CC and CP. Note however that anisotropy of GDLs has not been taken into account, and future work is needed to consider this important effect.

2.3. Boundary conditions

Eqs. (1)–(5), form a complete set of governing equations with nine unknowns: $\vec{u}$ (three components), P, C_{H_2}, C_{O_2}, C_{H_2O}, ϕ_e, and ϕ_s. Their corresponding boundary conditions are described as follows.

2.3.1. Flow inlet boundaries

The inlet velocity $\vec{u}_{\text{in}}$ in a gas channel is expressed by the respective stoichiometric flow ratio, i.e., ξ_a or ξ_c, defined at the average current density, I, as:

$$\xi_a = \frac{C^{H_2} u_{\text{in},a} A_a}{I A_{\text{mem}}/2F} \quad \text{and} \quad \xi_c = \frac{C^{O_2} u_{\text{in},c} A_c}{I A_{\text{mem}}/4F} \tag{16}$$

where A_a, A_c, and A_{mem} are the flow cross-sectional areas of the anode and cathode gas channels and the membrane area, respectively. The inlet molar concentrations are determined by the inlet pressure and humidity according to the ideal gas law.

2.3.2. Outlet boundaries

Fully developed or no-flux conditions are applied:

$$\frac{\partial \vec{u}}{\partial n} = 0, \qquad \frac{\partial C^k}{\partial n} = 0, \qquad \frac{\partial \phi_e}{\partial n} = 0, \qquad \frac{\partial \phi_s}{\partial n} = 0 \tag{17}$$
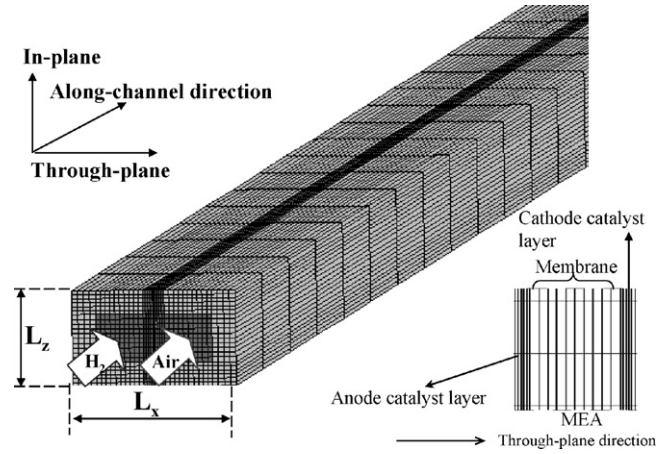

Fig. 3. Computational domain and mesh of a single-channel PEFC.

2.3.3. Walls

No-slip and impermeable velocity condition and no-flux condition are applied:

$$\vec{u} = 0, \qquad \frac{\partial C^k}{\partial n} = 0, \qquad \frac{\partial P}{\partial n} = 0, \qquad \frac{\partial \phi_e}{\partial n} = 0 \tag{18}$$

In addition, the boundary conditions for the electronic phase potential, ϕ_s, at the bipolar plate outer surfaces can be expressed as:

$$\begin{cases} \phi_s = 0, & \text{anode} \\ \dfrac{\partial \phi_s}{\partial n} = -\dfrac{I A_{\text{mem}}}{\sigma^{\text{eff}} A_{c,\text{wall}}}, & \text{cathode} \\ \dfrac{\partial \phi_s}{\partial n} = 0, & \text{otherwise} \end{cases} \tag{19}$$

where $A_{c,\text{wall}}$ is the area of the cathode outer surface.

2.4. Numerical procedures

The governing equations, Eqs. (1)–(5), along with their appropriate boundary conditions are discretized by the finite volume method [33] and solved by the commercial CFD software package, Fluent® (version 6.0.12), with SIMPLE (semi-implicit pressure linked equation) algorithm [33]. The SIMPLE algorithm is to update the pressure and velocity fields from the solution of the pressure correction equation, solved by algebraic multi-grid (AMG) method. Following the solution of the flow field, species, proton, and electron equations are solved. The source terms and physical properties are implemented in a user-defined functions (UDF) and the species and charge transport equations are solved through the software's user-defined scalars [34]. An average current density is specified as an input parameter, allowing the local current density and electronic phase potential to vary spatially according to local conditions. The mesh of a single-channel PEFC employed here for a numerical study is shown in Fig. 3 with the anode and cathode in co-flow. Geometrical and operating parameters of this PEFC are listed in Table 4. 120,000 ($60 \times 100 \times 12$) computational cells are used to capture the complex electrochemical and physical phenomena in the PEFC. In addition, in all the simulations to be presented
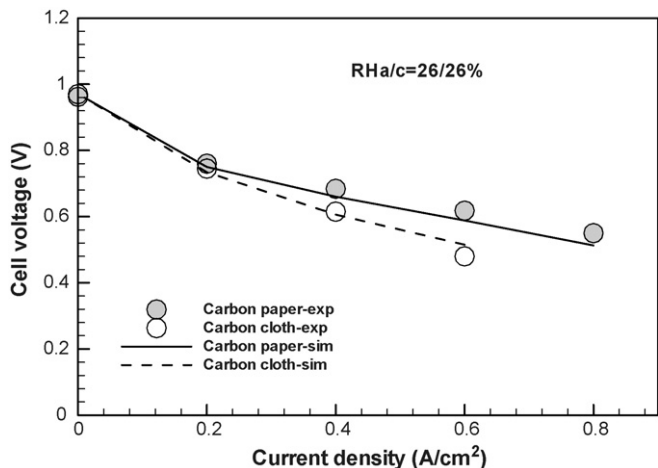
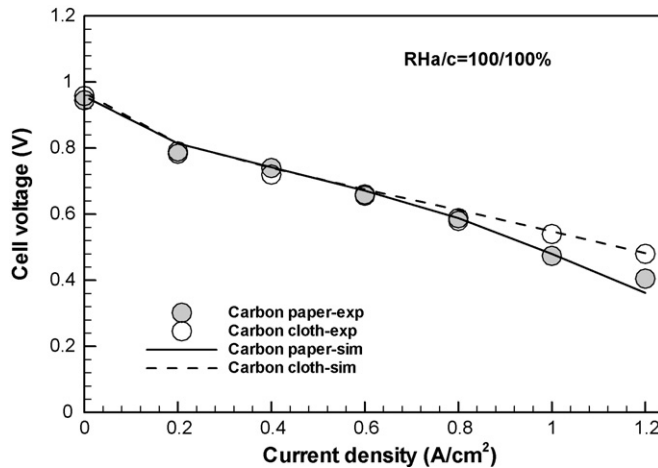Fig. 4. Polarization curves under low-humidity (RHa/c = 26/26%) operations.

Fig. 5. Polarization curves under full-humidification (RHa/c = 100/100%) operations.

in the next section, values of equation residuals are smaller than 10^{-6}.

3. Results and discussion

Validation of both low- and high-humidity operations, in the form of polarization curve, is presented in Figs. 4 and 5, respectively. Both figures show good agreement between simulation results and experimental data. It can be seen that under the low humidity, the CP exhibits better performance, while under the fully-humidified condition, the two materials perform the same at low current densities and the CC becomes superior when the current density is higher than 0.6 A/cm^2. A similar trend under high-humidity operations was also observed in the experiments of Ralph et al. [22]. To explore the fundamental differences between the two carbon substrates under dry and fully-humidified conditions, we focus on two cases with the average current density of 0.6 and 1.0 A/cm^2, respectively, in the following discussion.

Fig. 6 compares the oxygen concentration contours in the cathode GDL for the two substrates at 1.0 A/cm^2 and fully-humidified operation. It can be seen that the oxygen concentration in the CP is much lower than the one in the CC, indicative of the high transport resistance of the CP structure that is highly torturous. The limitation of oxygen transport is much more severe under the land as shown in this figure. Due to the domination of oxygen concentration polarization under high current densities, the CP shows lower performance as observed in Fig. 5.
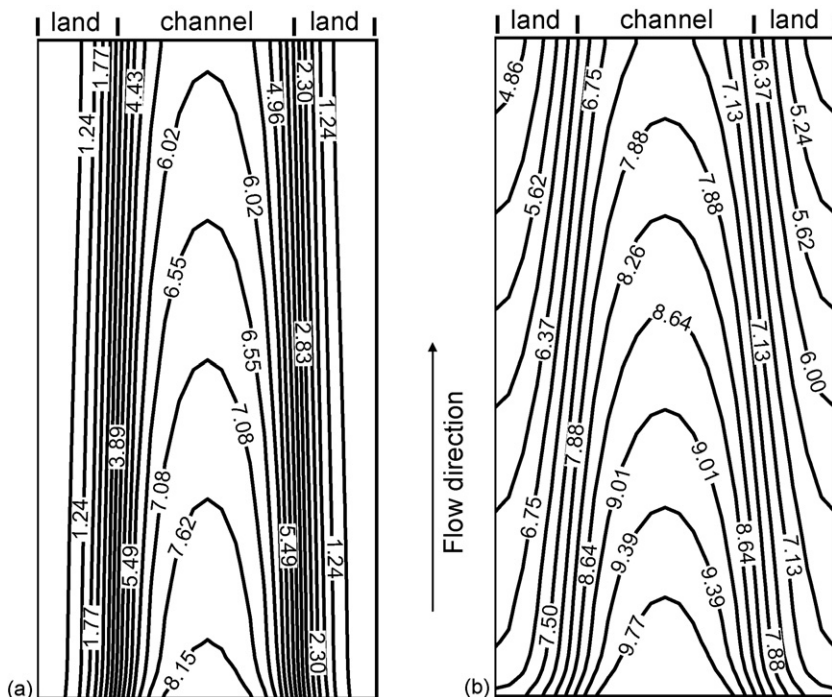

Fig. 6. Oxygen concentration distributions in the mid-section of the cathode GDL at 1.0 A/cm^2 and full-humidification: (a) carbon paper and (b) carbon cloth.
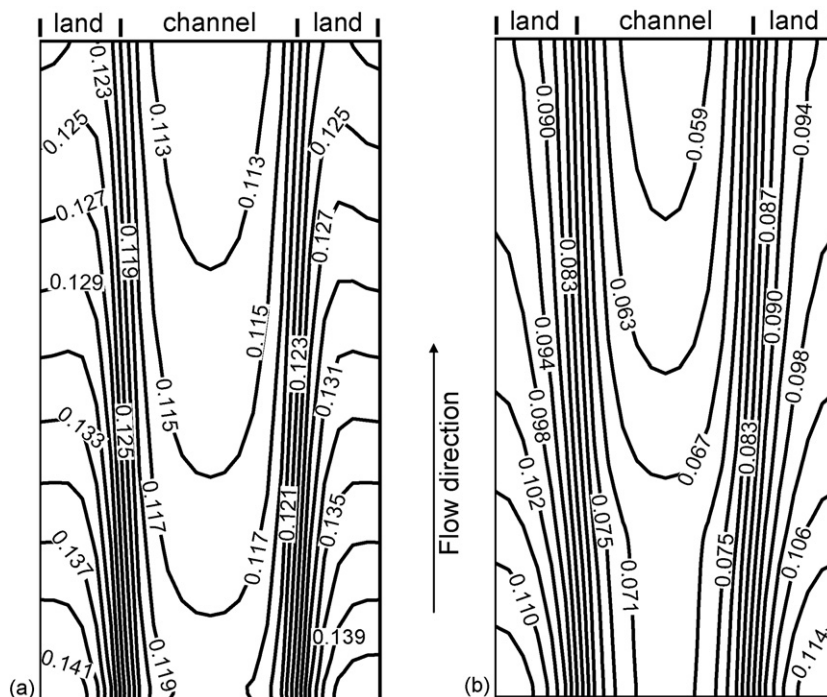
Fig. 7. Liquid water saturation (s) distributions in the mid-section of the cathode GDL at 1.0 A/cm^2 and full-humidification: (a) carbon paper and (b) carbon cloth.

Fig. 7 shows the contours of liquid water saturation in the same location and under the same operating conditions. It can be seen that the saturation level is lower in the CC, which can be explained by the fact that woven fabric surface is rougher and fibrous, and hence less liquid water coverage than the CP. Considering that liquid water hampers the oxygen gaseous transport, the higher saturation is also responsible for the lower oxygen

content in the CP as shown in Fig. 6. In addition, less water in the CC also raises less concern of liquid water covering the active catalyst surface.

Local performance of the cell at the same conditions can be quantitatively expressed by the density of protonic current across the membrane as shown in Fig. 8. It can be seen that the current density is more uniform for the CC. In addition, the CP shows
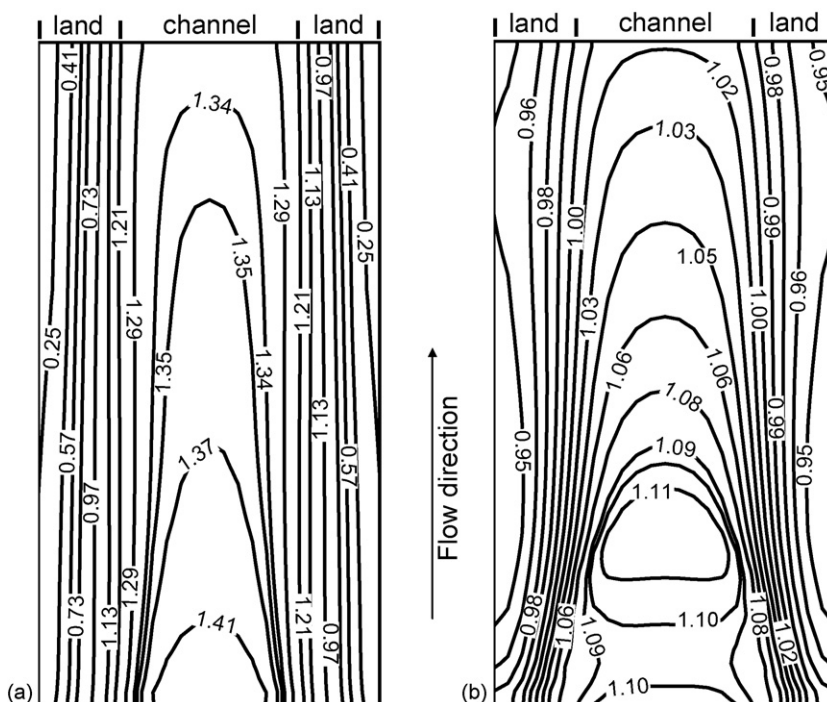

Fig. 8. Current density distributions in the mid-section of the membrane at 1.0 A/cm^2 and full-humidification: (a) carbon paper ($V_{cell} = 0.48$ V) and (b) carbon cloth ($V_{cell} = 0.545$ V).

higher current value under the channel because the carbon paper cell is subject to lower cell voltage as shown in Fig. 5, which leads to higher electrochemical surface overpotential. However, the current contribution under the land is much smaller for the CP substrate, which can be explained by the severe limitation of oxygen transport and high water coverage on the catalyst in the CP case. We can see that the structural difference between the two GDL materials results in more distinctive performance under the land portion, where the reactant transport resistance to the catalyst site is amplified. In addition, the higher current under the channel for the CP, observed in this figure, does not mean better local performance. This is due to the same average current density imposed, for which the CP allows more local current across the membrane (than the woven substrate) under the channel portion where the transport resistance is much smaller than under the land, comparing with the CC. In fact, by simple one-dimensional analysis, it can be shown that the CP is inferior to the CC under high-humidity operation considering its high mass transport resistance and water coverage. However, the impact of inferior factors varies in different regions of PEFCs, typically referred as to under the land and under the channel. Thus, a three-dimensional analysis can provide much more profound insight into the effect of structural differences between these two GDL substrates.

The above discussion links two structural factors of a GDL with cell performance, one is the GDL tortuosity, which affects species transports, and the other is the surface properties, i.e. the wettability and roughness, controlling water droplet attachment or water coverage on the GDL surface. The CP is inferior to the CC in both of these factors under high-humidify operations. Thus, the CP leads to lower performance as shown in Fig. 5.

This performance difference is significant under high current density operations dominated by mass transport polarization. The experiment conducted by Williams et al. [23] also shows the CP mostly is inferior under high-humidity operations. In addition, their fuel cells operate at the atmospheric pressure, which makes the mass transport limitation of the CP more severe.

The above evaluation is valid under high-humidity conditions, when the membrane is fully hydrated and hence the difference in membrane resistance between the two cases is negligible. As the gas humidity decreases, the ohmic resistance of the membrane begins to dominate cell performance in the intermediate range of the current density. Thus, the preference of GDL material properties shifts to the one leading to moisture preservation and high membrane hydration. Fig. 9 presents the water profiles in the cathode GDL for the two gas diffusion media under $0.6\,A/cm^2$ and low-humidity operation. It can be seen that the water concentration is much higher in the CP than the CC, which can be explained by the high tortuosity of the CC that prevents product water loss to the dry gas flows. The concentration difference is larger under the land. Accordingly, the membrane maintains a higher hydration level for the CP as shown in Fig. 10, which displays the water content, λ, in the membrane under the same condition. The water content contours directly reflect the protonic resistance distribution, keeping in mind that the membrane proton conductivity linearly increases with membrane water content, as suggested by Springer et al. [35] in Table 1.

Fig. 11 shows the oxygen concentration contours in the cathode GDL under the same condition. Similar to Fig. 6, lower oxygen concentration is present in the CP, indicative of the high tortuosity of its pore structure. However, the value of the oxy-
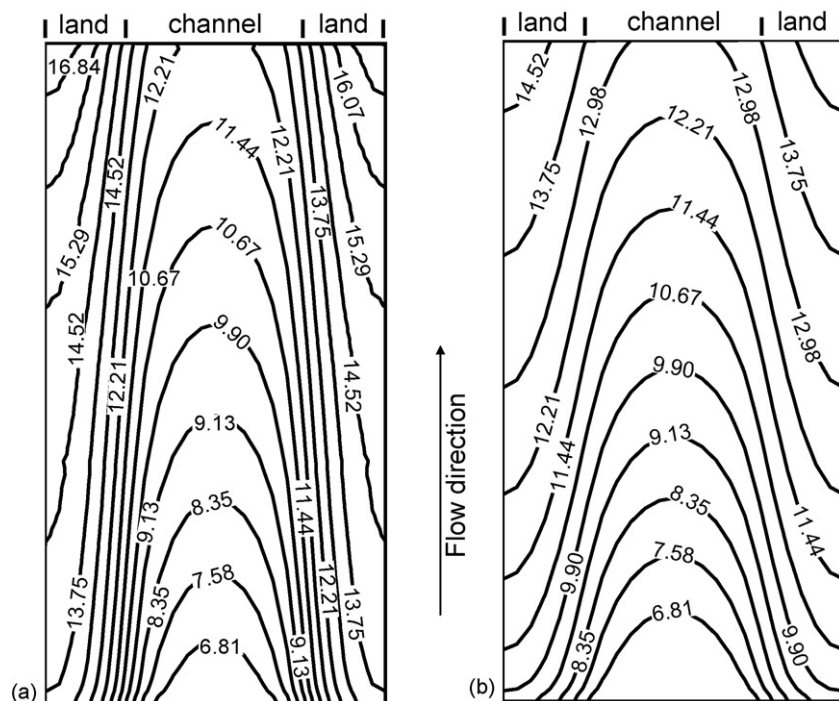

Fig. 9. Water concentration contours in the mid-section of cathode GDL at $0.6\,A/cm^2$ and low-humidity condition (RHa/c = 26/26%): (a) carbon paper and (b) carbon cloth.
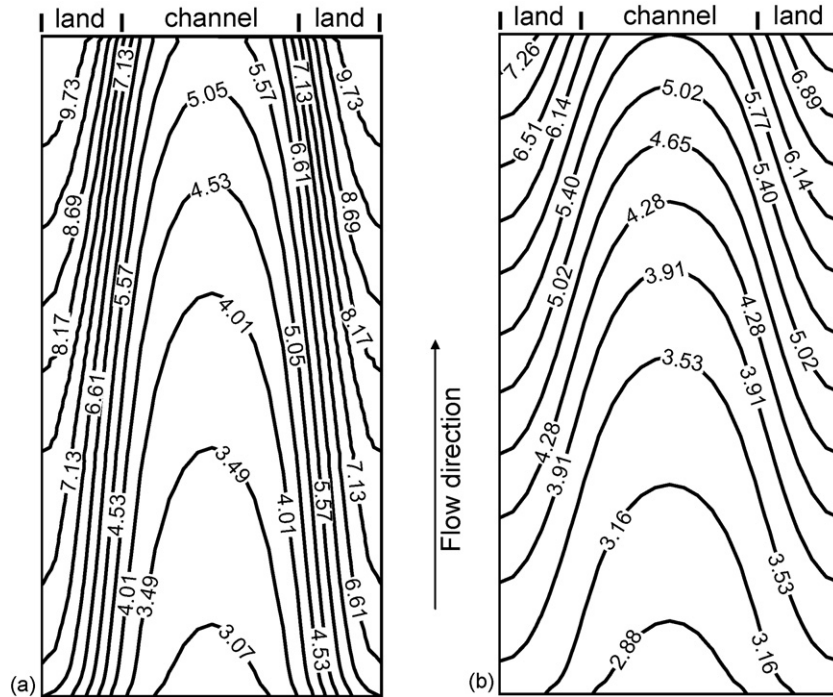
Fig. 10. Water content, λ, contours in the mid-section of the membrane at 0.6 A/cm² and low-humidity condition (RHa/c = 26/26%): (a) carbon paper and (b) carbon cloth.

gen content under the land is not as low as that in Fig. 6, which makes the mass transport polarization less important for this dry operation. Fig. 12 presents the current density distributions in the membrane for the two GDL substrates. It can be seen that high current density appears under the land for both GDL materials. This current distribution is usually indicative of the ohmic control of cell performance: higher water content appears under the land, improving the local proton conductivity and therefore high current flow across the membrane. Thus, in the dry operation, which is dominated by ohmic loss, the highly torturous structure of the CP helps membrane hydration and hence exhibit superior cell performance, as indicated by Figs. 10 and 4, respec-
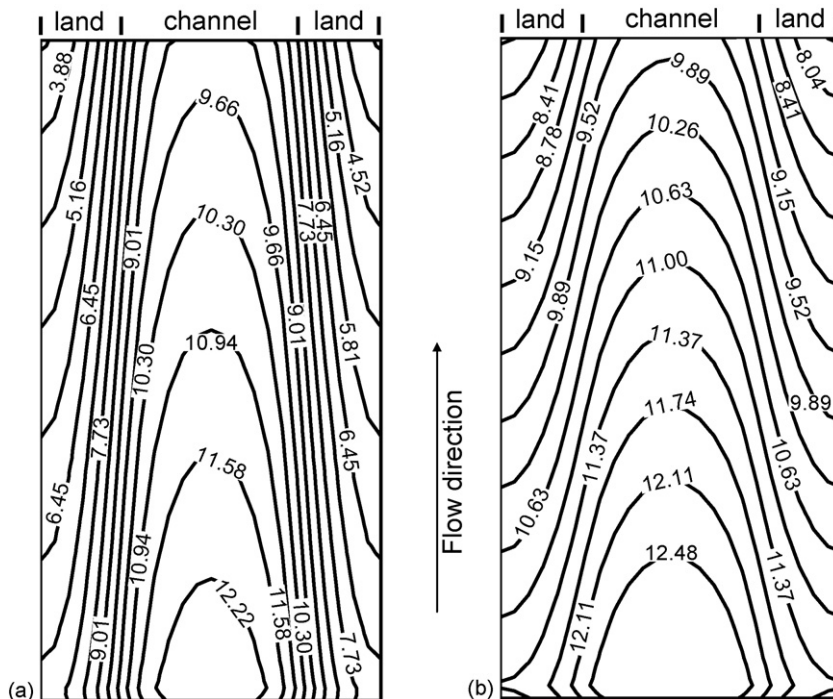

Fig. 11. Oxygen concentration contours in the mid-section of the cathode GDL at 0.6 A/cm² and low-humidity condition (RHa/c = 26/26%): (a) carbon paper and (b) carbon cloth.
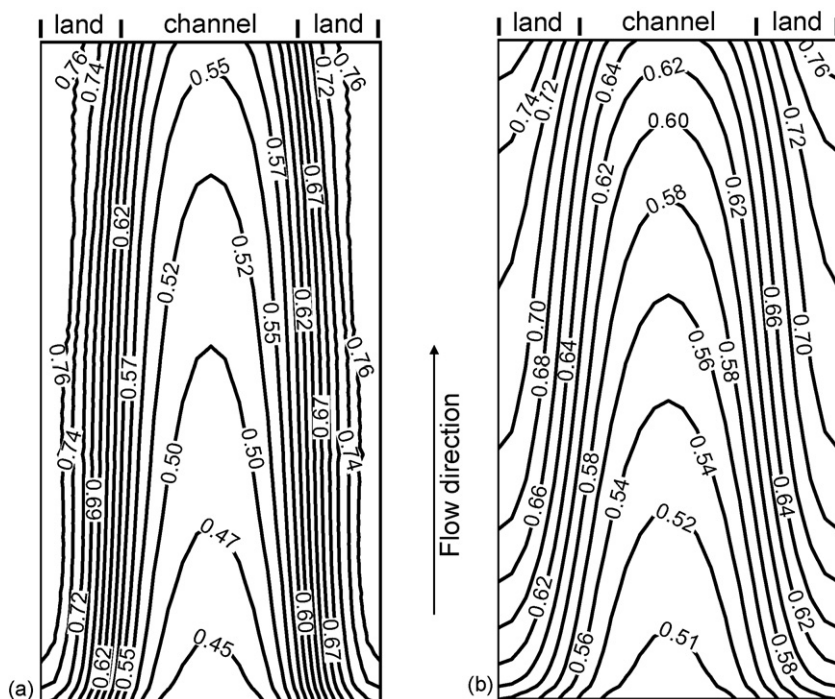
Fig. 12. Current density distributions in the mid-section of the membrane at 0.6 A/cm^2 and low-humidity condition (RHa/c = 26/26%): (a) carbon paper (0.585 V) and (b) carbon cloth (0.514 V).

tively. In addition, the performance difference in Fig. 4 occurs at the intermediate current density, which is typically the range of ohmic control. As the current density decreases, the difference vanishes.

4. Conclusions

A numerical study has been performed to examine the structure–performance relationship of carbon cloth and carbon paper as gas diffusion media of PEFCs. The structural characteristics of the two carbon substrates were incorporated into a multi-phase model and three-dimensional simulations were carried out to explore the fundamentals behind their performance differences under low- and high-humidity operations as observed experimentally. There exists good agreement between numerical and experimental data of polarization curves. Comparison of detailed water, oxygen, and current distributions with these two GDL materials indicates that highly tortuous structure of the carbon paper leads to severe mass transport limitation under high-humidity operations. In addition, its smooth surface makes water-droplet detachment difficult, resulting in severe water coverage on the surface and increased mass transport loss. Thus, the carbon cloth is a better choice as the GDL substrate for high-humidity operations. However, under the dry condition, the carbon paper is found to be superior due to its highly torturous pore structure, which retains product water in the MEA and improves the membrane hydration hence its proton conductivity. In addition, the two GDL materials display similar performance at low current densities controlled by the electrochemical kinetics.

Appendix A. Nomenclature

a	water activity; effective catalyst area per unit volume (m^2/m^3)
a_o	catalyst surface area per unit volume (m^2/m^3)
A	electrode area (m^2)
CC	carbon cloth
C^k	molar concentration of species k (mol/m^3)
c_p	specific heat (J/kg K)
CP	carbon paper
D	species diffusivity (m^2/s)
EW	equivalent weight of dry membrane (kg/mol)
F	Faraday's constant (96,487 C/equivalent)
i	superficial current density (A/cm^2)
I	current density (A/cm^2)
j	transfer current density (A/cm^3)
$\vec{j}_l$	mass flux of liquid phase (kg/m^2 s)

K	permeability (m^2)
k_r	relative permeability
L	length (m)
mf_l^k	mass fraction of species k in liquid phase
M	molecular weight (kg/mol)
n	the direction normal to the surface
n_d	electro-osmotic coefficient (H_2O/H^+)
P	pressure (Pa)
R	gas constant (8.134 J/mol K)
s	stoichiometry coefficient in electrochemical reaction or liquid saturation
S	source term
T	temperature (K)
$\vec{u}$	velocity vector (m/s)
U_o	equilibrium potential (V)
V_{cell}	cell potential (V)
X	mole fraction

Greek letters

α	transfer coefficient
ρ	density (kg/m^3)
μ	viscosity (kg/m s)
ν	kinematic viscosity (m^2/s)
θ_c	contact angle (°)
ϕ	phase potential (V)
κ	proton conductivity (S/m)
ξ	stoichiometric flow ratio
λ	membrane water content
λ_k	mobility of phase k
ε	porosity
η	surface overpotential (V)
τ	shear stress (N/m^2)
γ_c	correction factor for species convection
δ	thickness (m)
σ	electronic conductivity (S/m); or surface tension (N/m)

Superscripts and subscripts

a	anode
c	cathode; capillary
CL	catalyst layer
e	electrolyte
eff	effective value
g	gas phase
GDL	gas diffusion layer
in	inlet
k	species; liquid or gas phase
l	liquid
m	membrane phase
o	gas channel inlet value; reference value
ref	reference value
s	solid
sat	saturated value

References

[1] C.Y. Wang, Chem. Rev. 104 (2004) 4727.
[2] M. Mathias, J. Roth, J. Fleming, W. Lehnert, in: W. Vielstich, H. Gasteiger, A. Lamm (Eds.), Handbook of Fuel Cells: Fundamentals, Technology and Applications, vol. 3, John Wiley & Sons Ltd., 2003.
[3] J. Larminie, A. Dicks, Fuel Cell Systems Explained, John Wiley & Sons, 2000.
[4] J.S. Yi, T.V. Nguyen, J. Electrochem. Soc. 146 (1999) 38.
[5] Y. Wang, C.Y. Wang, J. Power Sources 147 (2005) 148.
[6] S. Dutta, S. Shimpalee, J.W. Van Zee, J. Appl. Electrochem. 30 (2000) 135.
[7] Y. Wang, C.Y. Wang, J. Electrochem. Soc. 152 (2) (2005) A445.
[8] S. Mazumder, J.V. Cole, J. Electrochem. Soc. 150 (2003) 1503.
[9] J.J. Hwang, J. Electrochem. Soc. 153 (2006) A216.
[10] Y. Wang, C.Y. Wang, J. Electrochem. Soc. 153 (2006) A1193.
[11] E. Birgersson, M. Noponen, M. Vynnycky, J. Electrochem. Soc. 152 (2005) A1021.
[12] U. Pasaogullari, C.Y. Wang, J. Electrochem. Soc. 151 (2004) A399.
[13] J.-H. Nam, M. Kaviany, Int. J. Heat Mass Transfer 46 (2003) 4595.
[14] D.M. Bernardi, M.W. Verbrugge, J. Electrochem. Soc. 139 (1992) 2477.
[15] H. Meng, C.Y. Wang, J. Electrochem. Soc. 151 (2004) A358.
[16] D. Bevers, R. Rogers, M. Von Bradke, J. Power Sources 63 (2) (1996) 193.
[17] X.-G. Yang, N. Burke, C.Y. Wang, K. Tajiri, K. Shinohara, J. Electrochem. Soc. 152 (2005) A759.
[18] G. Lin, T.V. Nguyen, J. Electrochem. Soc. 152 (2005) A1942.
[19] T. Zawodzinski, J. Bauman, F. Urbe, S. Gottesfeld, E.S. DeCastro, M. DeMarinis, in: S. Gottesfeld, T.F. Fuller (Eds.), Proceedings of the Second International Symposium on Proton Conducting Membrane Fuel Cells, Electrochemical Society, Pennington, NJ, 1999, p. 1, PV98-27.
[20] H.K. Lee, J.H. Park, D.Y. Kim, T.H. Lee, J. Power Sources 131 (1) (2004) 200.
[21] M.V. Williams, H.R. Kunz, J.M. Fenton, J. Power Sources 135 (2004) 122.
[22] T.R. Ralph, G.A. Hards, J.E. Keating, S.A. Campbell, D.P. Wilkinson, M. Davis, J. St-Pierre, M.C. Johnson, J. Electrochem. Soc. 144 (11) (1997) 3845.
[23] M.V. Williams, E. Begg, L. Bonville, H.R. Kunz, J.M. Fenton, J. Electrochem. Soc. 151 (2004) A1173.
[24] T. Frey, M. Linardi, Electrochim. Acta 50 (1) (2004) 99.
[25] Y. Wang, C.Y. Wang, J. Power Sources 153 (1) (2006) 130.
[26] C.Y. Wang, P. Cheng, Adv. Heat Transfer 30 (1997) 93.
[27] T. Berning, N. Djlali, J. Electrochem. Soc. 150 (2003) A1589.
[28] J. Benziger, J. Nehlsen, D. Blackwell, T. Brennan, J. Itescu, J. Mem. Sci. 261 (2005) 98.
[29] H. Meng, C.Y. Wang, J. Electrochem. Soc. 152 (2005) 1733.
[30] Y. Wang, C.Y. Wang, Electrochim. Acta 50 (2005) 1307.
[31] K.S. Chen, M.A. Hickner, D.R. Noble, Int. J. Energy Res. 29 (2005) 1113.
[32] F.Y. Zhang, X.G. Yang, C.Y. Wang, J. Electrochem. Soc. 153 (2006) A225.
[33] S.V. Patankar, Numerical Heat Transfer and Fluid Flow, Hemisphere Publishing Corp., New York, 1980.
[34] Fluent 6.1 UDF Manual, Fluent Inc., 2003.
[35] T.E. Springer, T.A. Zawodinski, S. Gottesfeld, J. Electrochem. Soc. 126 (1991) 2334.
[36] S. Motupally, A.J. Becker, J.W. Weidner, J. Electrochem. Soc. 147 (2000) 3171.
[37] T.A. Zawodzinski, J. Davey, J. Valerio, S. Gottesfeld, Electrochim. Acta 40 (1995) 297.
[38] A.C. West, T.F. Fuller, J. Appl. Electrochem. 26 (1996) 557.
[39] R.B. Bird, W.E. Stewart, E.N. Lightfoot, Transport Phenomena, John Wiley & Sons, New York, 2002.
[40] F.P. Incropera, D.P. DeWitt, Fundamentals of Heat and Mass Transfer, John Wiley & Sons, New York, 1996.